CONSORTIUM for BUILDING ENERGY INNOVATION

REPORT

Title: Improvements of Fast Fluid Dynamics for Simulating Airflow in Buildings

Report Date: January 2012

Report Author(s): Mingang Jin, Wangda Zuo, Qingyan Chen

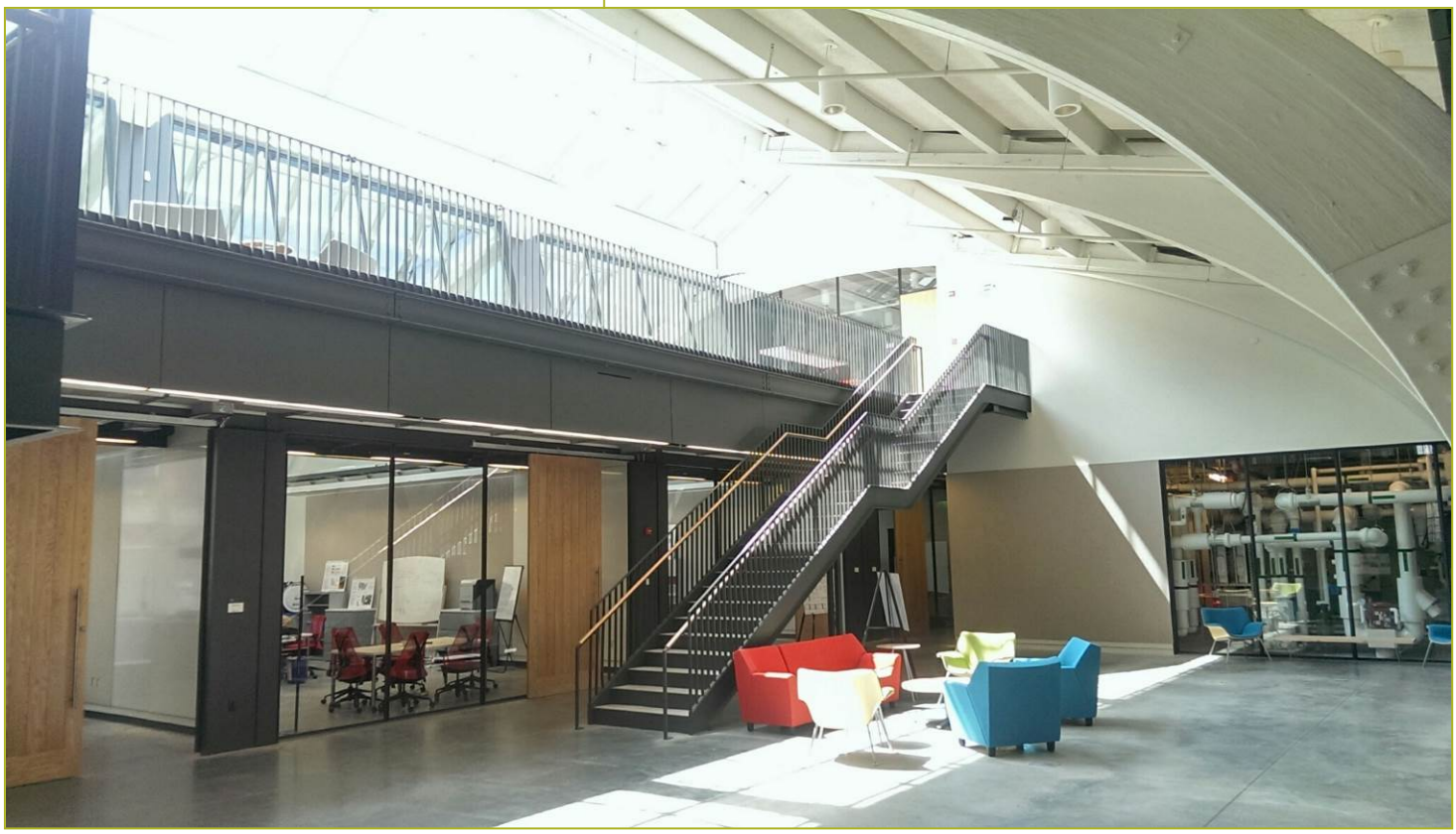

Funded by U.S. DOE

Report Abstract

Fluid Dynamics (FFD) could be potentially used for real-time indoor airflow simulations. This study developed two-dimensional Fast Fluid Dynamics (2D FFD) into three-dimensional Fast Fluid Dynamics (3D FFD) and improved the data structure for handling computational domain with more complex geometry.

Contact Information for Lead Researcher

Name: Qingyan Chen
Institution: Purdue University
Email address: yanchen@purdue.edu
Phone number: 765-496-7562

Acknowledgement

This material is based upon work supported by the Consortium for Building Energy Innovation (CBEI) sponsored by the U.S. Department of Energy under Award Number DE-EE0004261.

Jin, M, Zuo, W., and Chen, Q. "Improvements of fast fluid dynamics for airflow simulations in buildings," Submitted to *Numerical Heat Transfer*.

Improvements of Fast Fluid Dynamics for Simulating Airflow in Buildings

Mingang Jin[1], Wangda Zuo[2], Qingyan Chen[1]

[1]*School of Mechanical Engineering, Purdue University, West Lafayette, IN 47906, USA*

[2]*Environmental Energy Technologies Division, Lawrence Berkeley National Laboratory, Berkeley, CA 94720, USA*

Qingyan Chen (Corresponding Author)

Email: yanchen@purdue.edu

Phone: +1-765-496-7562

Fax: +1-765-494-0539

Abstract

Fast Fluid Dynamics (FFD) could be potentially used for real-time indoor airflow simulations. This study developed two-dimensional Fast Fluid Dynamics (2D FFD) into three-dimensional Fast Fluid Dynamics (3D FFD) and improved the data structure for handling computational domain with more complex geometry. The implementation of boundary condition at outlet was improved with local mass conservation method, and a near-wall treatment for Semi-Lagrangian scheme was applied to avoid having departure points located outside the boundary. This study tested 3D FFD with five cases of flow that have features of indoor airflow and compared the numerical results with corresponding reference data. The results show that the 3D FFD can successfully capture three dimensionality of the airflow and provide reliable and reasonably accurate simulations for flow in buildings with speed of about 15 times faster than current CFD tools.

Keywords: fast fluid dynamics; building airflow simulations; boundary condition; Semi-Lagrangian

NOMENCLATURE

Roman Symbols

F_i	body force
H	height
H	step height in of backward facing step
i, j	index of coordinate
$Mass_{in}$	total mass flow rate into the domain
$Mass_{out}$	total mass flow rate out the domain
N	index of boundary cell
n	previous time step
P	pressure
S	source term
T	temperature
t	time
U_i, U_j	velocity components in x_i and x_j directions, respectively
u	horizontal velocity component or velocity scale
v	vertical velocity component
W	width
w	velocity in the direction normal to the wall
x_i, x_j	spatial coordinates in i and j direction, respectively
x, y, z	spatial coordinates

z_0	coordinate of the wall
z_1	coordinate of the first grid adjacent to the wall
Δt	time step size
Δx, Δy	grid spacing size

Greek Symbols

Γ	transport coefficient
ρ	density
υ	kinetic viscosity
Φ	scalar in transport equation

1. Introduction

Buildings consume approximately 40 percent of primary energy in the United States and 70 percent of all electricity generated. Since high performance buildings can satisfy thermal comfort and indoor air quality while reducing energy use in buildings, such buildings are highly desired today. The design of high performance buildings often achieves energy reduction through optimal design and operation, which would require a tool that can be used to simulate quickly dynamic indoor environmental conditions.

Ideally, the simulations of dynamic indoor environmental conditions in a whole building should be performed in real time or faster-than-real-time. The real-time simulations would allow the building control systems to use the information for optimal control with minimal energy consumption. Although Computational Fluid Dynamics (CFD) has the potential to be used for the simulations, CFD is too slow with the present computing power in most of the design firms [1, 2]. Therefore, it is necessary to identify a suitable method that can be used to predict the dynamic indoor environmental conditions in a whole building in real time.

One of the possible methods is the multi-zone network models that could significantly decrease the computing time so that real time or faster-than-real-time simulations are possible. However, the well mixing assumption of the indoor airflow used in the multi-zone method is not always valid, such as for large indoor spaces or rooms with stratified ventilation systems [2]. In these cases, the multi-zone models may predict inaccurate results [3]. The multi-zone model also uses only one node for a room that provides insufficient information of the micro environment, which is critical for thermal comfort and air quality.

The other possible method for real-time indoor environment simulations is Fast Fluid Dynamics (FFD). The method, originally used from computer games, could be used for the simulations of indoor environmental conditions. Zuo et al. [4, 5] developed a two-dimensional Fast Fluid Dynamics (2D FFD) for airflow simulations in buildings. Their results show that the computing speed was 50 times faster than CFD and real-time simulation of indoor airflow seems possible. Although the results were not as accurate as those of CFD, they were much better than those produced by the multi-zone model.

However, flows in buildings are complex and always three dimensional [6]. In order to capture the characteristics of the three-dimensional airflows, it is necessary to extend the 2D FFD code into a three dimensional one. To demonstrate the capabilities and accuracy of the 3D FFD code, it is essential to apply it to a few cases of indoor airflows with high quality reference data. This forms the basis of current investigation reported in this paper.

2. Research Method

The following section discussed the fundamentals of FFD, the implementation of 3D FFD, and how our 3D FFD code handled different boundary conditions normally encountered in indoor environment.

2.1 Governing equations for fast fluid dynamics

Fast Fluid Dynamics (FFD) is a technique introduced by Stam [7] for computer games, aimed to simulate incompressible fluid flows with a simple and stable approach. In fact, FFD is a form of projection method introduced by Chorin [8] in early 1960s to solve the incompressible Navier-Stokes (NS) equations (1) and continuity equation (2) given below.

$$\frac{\partial U_i}{\partial t}+U_j\frac{\partial U_i}{\partial x_j}=-\frac{1}{\rho}\frac{\partial p}{\partial x_i}+\upsilon\frac{\partial^2 U_i}{\partial x_j\partial x_j}+\frac{1}{\rho}F_i \tag{1}$$

$$\frac{\partial U_i}{\partial x_i}=0 \tag{2}$$

Where U_i and U_j are velocity, p pressure, ρ density, F_i body forces, and x_i and x_j spacial coordinates, respectively. In the projection method, instead of solving a coupled system of Navier-Stokes equations for velocity and pressure, typically a sequential two-stage method is applied. At first, an intermediate velocity field is computed from the momentum equations ignoring the incompressibility constrain, and then pressure projection is used to project the intermediate velocity field into a space of divergence free vector field to obtain pressure and updated velocity. However in FFD, a three-step method is used by solving the following three equations in each step:

$$\frac{U_i^*-U_i^n}{\Delta t}=-U_j\frac{\partial U_i}{\partial x_j} \tag{3}$$

$$\frac{U_i^{**}-U_i^*}{\Delta t}=\upsilon\frac{\partial^2 U_i}{\partial x_j\partial x_j}+\frac{1}{\rho}F_i \tag{4}$$

$$\frac{U_i^{n+1}-U_i^{**}}{\Delta t}=-\frac{1}{\rho}\frac{\partial p}{\partial x_i} \tag{5}$$

Where, U^n and U^{n+1} represents velocity at previous time step and current time step, respectively, and U^* and U^{**} are intermediate velocities. At the first step, FFD uses the first-order Semi-Lagrangian scheme to solve equation (3) for convection, and the velocity at previous time step is updated with U^*. At the second step, the fully implicit scheme is used to solve equation (4) for the diffusion with the source term, and the intermediate velocity is further updated with U^{**}. At the third step, the pressure projection is conducted. From equations (2) and (5), it is easy to derive the following Poisson equation (6).

$$\frac{\partial^2 p}{\partial x_j\partial x_j}=\frac{\rho}{\Delta t}\frac{\partial U_i^{**}}{\partial x_i} \tag{6}$$

The pressure obtained from solving the Poisson equation is then used to update velocity field with equation (5). After obtaining the velocity field, transport equations (7) for other scalars can be further solved similarly.

$$\frac{\partial \Phi}{\partial t}+U_j\frac{\partial \Phi}{\partial x_j}=\Gamma\frac{\partial^2 \Phi}{\partial x_j\partial x_j}+S \tag{7}$$

Where, Φ is the scalar to be solved, Γ the transport coefficient, and S source term, respectively.

2.2 Implementation of the three dimensional code

The extension from the 2D FFD to the 3D FFD was straightforward as all the governing equations were identical. The 3D FFD used a finite-volume discretization scheme, which essentially satisfied conservation laws. The 3D FFD also applied staggered grid [9] to store velocity on the grid faces and other variables at the grid center as shown in Figure 1.

In addition, the 3D FFD code introduced different markers for identifying boundary cells and interior cells to handle complex geometry. As illustrated in Figure 2, cells in the interior of the fluid region were assigned value 1 to a marker, and cells at the boundary with grey colour were marked as 0. With this approach, the code could automatically identify boundary cells and interior cells during computation, which would deal with obstacles flexibly in the computational domain.

2.3 Implementation of boundary conditions

Proper boundary conditions are crucial in solving incompressible Navier-Stokes equations [10]. In FFD, paired boundary conditions for both velocity and pressure are required to solve implicit diffusion equations and Poisson equation [11,12]. Different velocity and pressure boundary conditions would be assigned for different type of boundaries. For airflow simulations in buildings, the computation domains are typically bounded by solid walls and openings, such as inlets and outlets. For the solid walls, non-slip boundary is usually applied. For inlets, constant velocity is enforced. Both of these two boundary conditions can be categorized as Dirichlet boundary. As equation (8) shows, the 3D FFD used the physical velocity boundary condition as boundary condition for intermediate velocity. The Neumann boundary condition for pressure was derived from equations (5) and (8) to form equation (9).

$$U_i^{**}|_b = U_i^{n+1}|_b = U_{bi} \tag{8}$$

$$\frac{\partial p}{\partial n}|_b = 0 \tag{9}$$

At outlets, usually outflow boundary condition is applied; however, the implementation of outflow boundary condition in FFD can be done in multiple ways. The most common approach of the velocity at outflow boundary is a simple Neumann boundary condition with its gradient set to be zero. This approach is based on the assumption that the outlet is located at fully developed region while in building airflow simulations this is usually not the case, because the location of outlet is often at circulation region. Therefore, this investigation applied the local mass conservation for the outflow boundary conditions for velocity as suggested by Li et al. [13].

Figure 3 illustrated the implementation of local mass conservation method. The normal derivative of tangential velocity at the outlet was set to zero. The velocity component normal to the outlet was firstly derived by applying mass conservation at the cells adjacent to the outlet, as shown in equation (10).

$$u_{N,j} = u_{N-1,j} + \frac{\Delta x}{\Delta y}(v_{N,j-1} - v_{N,j}) \tag{10}$$

However the boundary velocity derived from equation (10) would not ensure overall mass conservation. This study further corrected the boundary normal velocity through mass correction equation (11).

$$u_{N,j} = u_{N,j} \times \frac{Mass_{in}}{Mass_{out}} \tag{11}$$

Where, $Mass_{in}$ is the total mass-flow rate at all the inlets and $Mass_{out}$ the total mass-flow rate at all the outlets, respectively. Since the mass conservation constraint had already been applied at the outlet boundary cells, it was not necessary to update the normal velocity at the outlet boundary through pressure projection. Similarly, Neumann boundary conditions could be derived for pressure at outflow boundaries as shown by equation (9).

2.4 Treatment of Semi-Lagrangian scheme at near-wall regions

FFD used Semi-Lagrangian scheme [14] for solving the advection equations. Figure 4 demonstrated the principle of Semi-Lagrangian scheme. The backward trajectory approach was designed to determine the departure locations of particles that arrive at grid points at the new time step. The velocity and other scalars at the departure point could be interpolated from those known at surrounding grid cells.

Note that only the first-order time accuracy can be obtained by the one-time-step Semi-Lagrangian scheme. The truncation error might lead to a high probability that the tracing back from the arrival location near a solid wall could be located outside of the flow domain, as depicted in Figure 5(a). The FFD would then relocate any departure point outside the boundary to the nearest wall boundary, but this might result in too low velocity in the domain where many departure points were located on the solid wall boundary [15].

In order to avoid having departure points located outside the boundary, the 3D FFD employed a special treatment for the Semi-Lagrangian scheme at the near wall region. The treatment assumed that the velocity component normal to the wall varied linearly between the wall boundary and the first grid adjacent to the wall, as shown in Figure 5(a). If the backward trajectory crossed the first grid close to the wall boundary, the tracing back velocity in the normal wall direction would linearly decrease to zero at wall surface. Thus the departure point would not locate outside the domain.

As illustrated in Figure 5(b), the trace back in the normal wall direction (z direction) was first performed with velocity at arrival point, which was w_a. Once the trace back trajectory crossed the first grid adjacent to the wall, the equation (12) was used for trace back velocity, w.

$$w=\frac{z-z_0}{z_1-z_0}w_1 \tag{12}$$

where, z is coordinate in normal wall direction, z_0 the coordinate of wall boundary in normal wall direction, z_1 the coordinate of first grid adjacent to wall in normal wall direction and w_1 the velocity at the point where the trajectory crossed the first grid adjacent to the wall, respectively. The equation (12) was then integrated over the remained trace-back time to derive the coordinate of departure point, as shown by equation (13).

$$z_d=z_0+(z_1-z_0)\exp\left[-\frac{v_1}{z_1-z_0}(\Delta t-\frac{z_a-z_1}{w_a})\right] \tag{13}$$

Where z_d is the coordinate of departure point in normal wall direction, z_a the coordinate of arrival point in normal wall direction and Δt the time step size, respectively.

3. Results

With the numerical method outlined in the previous section, this investigation evaluated the performance of the 3D FFD for five cases with reference data available from the literature. The cases are: (1) a simple lid driven cavity flow that shows a typical room

airflow pattern with mixing ventilation by a wall jet, (2) a backward facing step flow that looks like a jet coming from a duct to a room, (3) a forced convection flow in empty room that is more realistic in buildings, (4) a forced convection flow in a room with a box that represents a piece of furniture, and (5) a mixed convection flow in a room with a heated box that represents occupant or heated equipment.

3.1 Case 1: Airflow in a lid driven cavity

The lid-driven cavity flow is one of the most important benchmark cases for numerical solvers of Navier-Stokes equation. The flow has a simple computational domain of square geometry and single driving force by means of tangential movement of the lid with constant velocity. Thus only Dirichlet boundary conditions for velocity were applied in the 3D FFD. Ku et al. [16] studied the three dimensional lid driven cavity flows with Chebyshev pseudo-spectral technique and found that the flow was more affected by three dimensional boundaries with increasing Reynolds number from 100 to 1000. As shown in Figure 6, this investigation used the similar cubic cavity as Hwar et al. [16] for the test case. The size of the cavity was 1 m × 1 m × 1 m and the Reynolds number based on the cavity dimension was 1000. In order to access the capability of the 3D FFD in predicting the three dimensional flows, both 3D FFD and 2D FFD were used to simulate the airflow with the grid size of 60×60×60 and 60×60, respectively.

Figure 7 compared velocity profiles simulated by 2D FFD and 3D FFD at the vertical and horizontal centerline of the cavity. The high accuracy simulation data from Ku et al. [16] was used as a reference. Figure 7(a) showed that 2D FFD obtained a higher peak velocity at Y/L=0.2 and higher velocity at Y/L=0.8 than 3D FFD and reference data, because 2D FFD could not predict viscous effect from the side walls. Also the viscous effect was the same reason that 2D FFD predicted an average higher velocity value at the center region of cavity than 3D FFD and reference data in Figure 7(b). However, because of the existence of numerical diffusivity in FFD, there was some discrepancy between the results of 3D FFD and reference data. For instance, in Figure 7(a), the velocity at Y/L=0.4 was under-predicted by 3D FFD, and in Figure 7(b), the peak velocity near both right and left wall were also under-estimated by 3D FFD. Overall, the result from 3D FFD was more accurate than 2D FFD, because it was able to predict the three dimensionality of airflow cased by side wall effect.

3.2 Case 2: Airflow through backward facing step

Backward facing step flow comprises separation, recirculation, and subsequently reattachment, which are fundamental features of complex airflow in buildings, and also have both openings and walls, so this would be a good test case for 3D FFD before it was tested for real flows in buildings. Armaly et al. [17] conducted experimental investigation of backward-facing step flow and high quality data was obtained. This study applied the same settings as in the experiment by Armaly et al. [17] for the test case. As depicted in Figure 8, the channel height in the upstream of the step, h, was 5.2 mm and the downstream channel height, H, was 10.1 mm, giving the expansion ratio of 1.94. The width of the channel, W, was 180 mm, giving the aspect ratio of 18:1. At the inlet, fully developed velocity profile was applied for velocity boundary condition and outflow boundary condition was used at the downstream outlet. Similar to the previous test case, both 2D FFD and 3D FFD were applied to simulate the flow features in the backward facing step. The grid size of 40×40×20 and 40×20 was used for 3D FFD and 2D FFD, respectively.

Figure 9 showed the dependence of the normalized primary reattachment length on Reynolds number. The result from 2D FFD and 3D FFD results are compared with

experimental data from Armaly et al. [16]. At low Reynolds numbers, both 3D FFD and 2D FFD results had excellent agreement with the experimental data. However, when the Reynolds number became higher than 400, the 3D FFD results still agree with the experimental data, but the 2D FFD results diverged from the data. As pointed out by Armaly et al. [17], at higher Reynolds number, the sidewall of the channel would induce three dimensionality of the flow, affecting the flow structure at the channel mid-plane. Obviously, 2D FFD was incapable to include the three-dimensional features.

3.3 Case 3: Forced convection in the empty room.

In order to evaluate 3D FFD for more realistic cases, this study tested 3D FFD with cases from Wang et al. [18]. They investigated experimentally the airflows with adding features in a room: (A) isothermal forced convection in the empty room; (B) isothermal forced convection in the room with a box; (C) mixed convection in the room with the heated box.

Figure 10 showed the case of forced convection in the empty room. An isothermal jet was generated at the inlet at upper left corner and developed along the ceiling, reaching far right. The air then turned downwards because of the existence of right wall and further formed a circulation in the room. This was a basic airflow pattern in a mechanically ventilated room. The room size was 2.44 m × 2.44 m × 2.44 m and the inlet and outlet height was 0.03 m and 0.08 m, respectively. The inlet air velocity was 0.455 m/s with the corresponding Reynolds number around 2,000. The local mass conservation method was applied at the outlet. In order to compare the performance of 3D FFD with CFD tools, the laminar CFD simulation using ANSYS Fluent 12.1 was also performed for this test case. The grid size of 20×20×20 was used for both 3D FFD and laminar CFD calculations.

Figure 11 showed the velocity profiles at four measurement positions predicted by 3D FFD and laminar CFD. As depicted in Figure 10, the four positions were 1, 3, 5 and 6 located at the jet upstream, jet downstream, room center and a position close to the side wall, respectively. Figure 11 showed that 3D FFD predicted similar airflow as the laminar CFD in this case. Both of them could predict general velocity variation in the vertical direction and capture the high speed of the jet from inlet. Their results matched with experimental data quite well at position 3, located in the center of the room. At near-wall region with relatively high gradient (position 5), both 3D FFD and laminar CFD could not obtain a good agreement with the experiment data. Similarly, Wang et al. [18] also found that the CFD simulation with turbulence models did not do a good job at position 5. This was because the flow structure was much complex near the right wall, where separation occurred.

3.4 Case 4: Forced convection in the room with box.

This test case was Case B from Wang et al. [18]. As illustrated in Figure 12, a box was added in the center of the room, and it would cause airflow separation that was similar as the airflow in a room blocked by obstacles like furniture and occupants. So in this case, 3D FFD could be further tested with increasing airflow features and more complex geometry of computational domain. The room size was identical with the one in previous case, and the dimension of box was 1.22 m × 1.22 m × 1.22 m. The inlet and outlet boundary conditions were also the same with the settings in the previous case. Similarly, this test case was also simulated with laminar CFD using ANSYS FLUENT 12.1[19], and the grid size of 20×20×20 was used for both 3D FFD and laminar CFD simulations.

Figure 13 reported the velocity profiles at the four locations predicted by 3D FFD and laminar CFD simulations. The results were compared with the experiment data from Wang et al. [18]. 3D FFD under predicted the air velocity at position 1 and 5, because the airflow was complex at position 5, where the airflow was blocked by the box and formed a secondary circulation between the box and right wall. Also this under-prediction might imply that the current scheme is so diffusive that the air velocity affected a lot by the solid wall. At other two positions the agreement was acceptable with only some discrepancies at near-floor-region. Compared with the results of laminar CFD simulation, 3D FFD was better for this case.

3.5 Case 5: Mixed convection in the room with box.

In Case C from Wang et al. [18], a heat source of 700W was added in the box in Case B. The heated box would generate thermal plumes as often found from different heating sources in buildings, such as occupants and electric appliances, etc. The supply air temperature was controlled at 22.2 ^{o}C; the temperature of box surface, ceiling, surrounding walls and floor were 36.7, 25.8, 27.4 and 26.9 ^{o}C, respectively. All other boundary conditions were the same as Case B. The grid size of $20 \times 20 \times 20$ was used for both 3D FFD and laminar CFD simulation in this case.

In Figure 14, the vertical velocity profiles predicted by 3D FFD showed very good agreement with the experimental data except at position 5. Similar to Case B, the failure of 3D FFD at position 5 might caused by its incapability of modeling complex flow structure. Compared with the results of CFD simulations, 3D FFD obtained more accurate results than laminar CFD.

This case was non-isothermal so the temperature profiles predicted was compared with the experimental data in Figure 15 at the four positions. The temperature was normalized and defined as $T^*= (T-T_{min})/ (T_{max}-T_{min})$, where T_{min} = 22.2^{o}C and T_{max} = 36.7 ^{o}C were the minimum and maximum temperature found in this case, respectively. At these positions, although the result of 3D FFD was not in perfect agreement with the experimental data, it was still acceptable that it predicted correct temperature magnitude and captured the general vertical variation of temperature. Because of lack of turbulence model, the laminar CFD could not predict the surface heat transfer coefficient correctly and thus under predicted the temperature magnitude. While in 3D FFD, an ad-hoc treatment was applied to adjust the surface heat transfer coefficient so 3D FFD could achieved a better prediction for temperature than laminar CFD.

4. Discussions

Through the tests above, it proved that 3D FFD was reasonably accurate and reliable for simulating airflows in buildings. Although the main objective of 3D FFD was not to pursue accuracy, the comparison with results of laminar CFD showed that the overall performance of 3D FFD in simulating real flow in the last three cases was better. This seemed a little strange because no turbulence models were used in current 3D FFD. The possible explanation was that the numerical viscosity generated by FFD scheme acted as adding turbulent viscosity into the flows and thus predicted more realistic flows. However, not in all cases, numerical viscosity would positively affect airflow simulations. In lid driven cavity, the FFD scheme was so diffusive that under-predicted the peak velocities.

The major advantage of the FFD compared to CFD is its speed. This study also conducted a comparison of simulation speed between 3D FFD and laminar CFD. Table

1 reported the computing time of the test cases. All three cases used same time step size of 0.1 seconds and grid size of $20\times20\times20$, and both 3D FFD and laminar CFD simulations were performed on a personal computer with a single Intel CPU at 3.00 GHz. Comparing the elapsed flow time and the elapsed CPU time, 3D FFD could realize faster-than-real time simulations for the grid size and time steps. On the other hand, laminar CFD was 14-18 times slower than 3D FFD.

5. Conclusion

It is essential to extend the capability of fast fluid dynamics in modelling three dimensional flows before its application in building airflow simulations. In this paper, the three dimensional fast fluid dynamics (3D FFD) was developed from a previously developed two dimensional model.

The 3D FFD adopted the finite volume discretization scheme on staggered grid, and improved the data structure to handle computational domain with more complex geometry. Local mass conservation method was applied to improve the implementation of boundary condition at outlet. This study also proposed approximation on near wall treatment for Semi-Lagrangian scheme to avoid having departure points located outside the boundary.

Through the tests of lid-driven cavity and backward facing step, 3D FFD successfully predicated the side-wall viscous effect and proved its capability of capturing three dimensionality of air flow. So, 3D FFD could achieve higher accuracy than 2D FFD on modelling the three dimensional flows.

The 3D FFD was also tested for more realistic flows in buildings, which covered flow features including jet flow, flow separation and thermal plumes, etc. The results showed that 3D FFD could provide reliable and acceptably accurate simulations for building airflows. The computing speed was about 15 times faster than CFD.

References

[1] Z. Zhai and Q. Chen, Sensitivity analysis and application guides for integrated building energy and CFD simulation, *Energy and Buildings*, vol. 38, pp. 1060-1068, 2006.

[2] Q. Chen, Ventilation performance prediction for buildings: A method overview and recent applications, *Building and Environment*, vol. 44, pp. 848-858, 2009.

[3] L. Wang and Q. Chen, Evaluation of some assumptions used in multizone airflow network models, *Building and Environment*, vol. 43, pp. 1671-1677, 2008.

[4] W. Zuo and Q. Chen, Real‐time or faster‐than‐real‐time simulation of airflow in buildings, *Indoor Air*, vol. 19, pp. 33-44, 2009.

[5] W. Zuo and Q. Chen, Fast and informative flow simulations in a building by using fast fluid dynamics model on graphics processing unit, *Building and Environment*, vol. 45, pp. 747-757, 2010.

[6] Z. Zhai, W. Zhang, Z. Zhang, and Q. Chen, Evaluation of Various Turbulence Models in Predicting Airflow and Turbulence in Enclosed Environments by CFD: Part 1--Summary of Prevalent Turbulence Models, *HVAC&R Research*, vol. 13, pp. 853-870, 2007.

[7] J. Stam, Stable fluids, *The 26th annual conference on Computer graphics and interactive techniques*, Los Angeles, 1999, pp. 121-128.

[8] C. Alexandre, A numerical method for solving incompressible viscous flow problems, *Journal of Computational Physics*, vol. 2, pp. 12-26, 1967.

[9] F. H. Harlow and J. E. Welch, Numerical Calculation of Time-Dependent Viscous Incompressible Flow of Fluid with Free Surface, *Physics of Fluids*, vol. 8, p. 2182, 1965.
[10] D. Rempfer, On Boundary Conditions for Incompressible Navier-Stokes Problems, *Applied Mechanics Reviews*, vol. 59, pp. 107-125, 2006.
[11] Y. B. Kim and M. J. Lee, Boundary-condition pairs for fractional step methods and compatibility with the pressure Poisson equation, *Computational Fluid Dynamics Journal*, vol. 11, pp. 323-334, 2002.
[12] R. Temam, Remark on the pressure boundary condition for the projection method, *Theoretical and Computational Fluid Dynamics*, vol. 3, pp. 181-184, 1991.
[13] P. W. Li and W. Q. Tao, Effects of outflow boundary condition on convective heat transfer with strong recirculating flow, *HEAT AND MASS TRANSFER*, vol. 29, pp. 463-470, 1994.
[14] A. Staniforth and J. Côté, Semi-Lagrangian Integration Schemes for Atmospheric Models—A Review, *Monthly Weather Review*, vol. 119, pp. 2206-2223, 1991.
[15] N. Wood, A. Staniforth, and A. White, Determining near‐boundary departure points in semi‐Lagrangian models, *Quarterly Journal of the Royal Meteorological Society*, vol. 135, pp. 1890-1896, 2009.
[16] H. C. Ku, R. S. Hirsh, and T. D. Taylor, A pseudospectral method for solution of the three-dimensional incompressible Navier-Stokes equations, *Journal of Computational Physics*, vol. 70, pp. 439-462, 1987.
[17] B. F. Armaly, F. Durst, J. C. F. Pereira, and B. Schönung, Experimental and Theoretical Investigation of Backward-Facing Step Flow, *Journal of Fluid Mechanics*, vol. 127, pp. 473-496, 1983.
[18] M. Wang and Q. Chen, Assessment of various turbulence models for transitional flows in an enclosed environment, *HVAC&R Research*, vol. 15, pp. 1099-1119, 2009.
[19] ANSYS, ANSYS FLUENT 12.1 Documentation, ANSYS Inc., PA.

Table 1 Comparison of computing time by 3D FFD and laminar CFD

Test cases	Elapsed flow time (s)	Elapsed CPU time (s)	
		3D FFD	CFD
Forced convection in empty room	100	29	474
Forced convection in room with box	100	31	439
Mixed convection in room with box	100	31	555

Figures

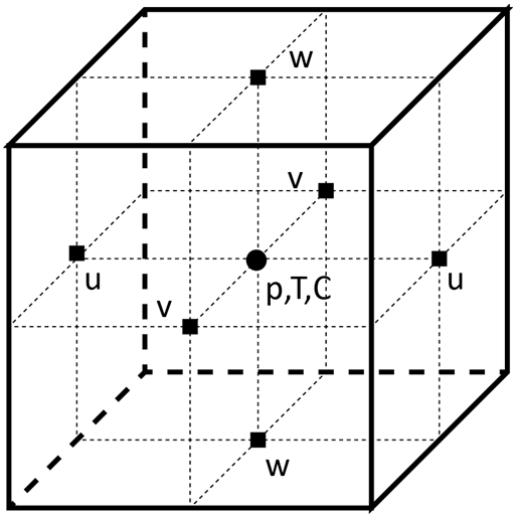

Figure 1 The schematic of a staggered grid

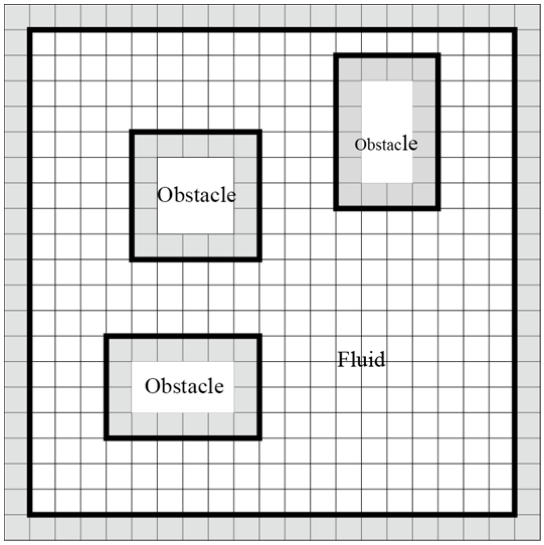

Figure 2 The boundary cells and interior cells in the computational domain

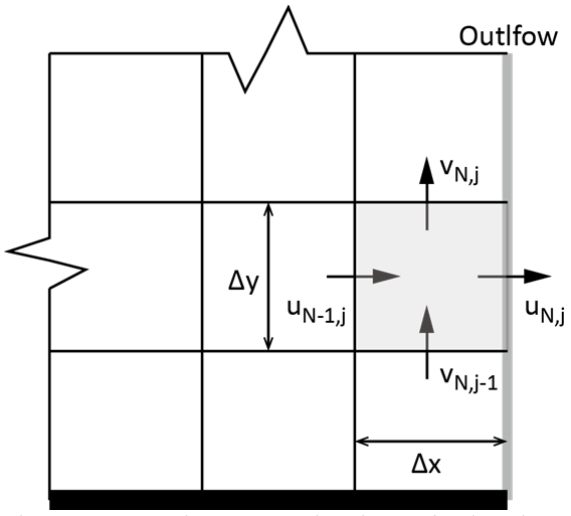

Figure 3 Boundary control volume for local mass conservation method

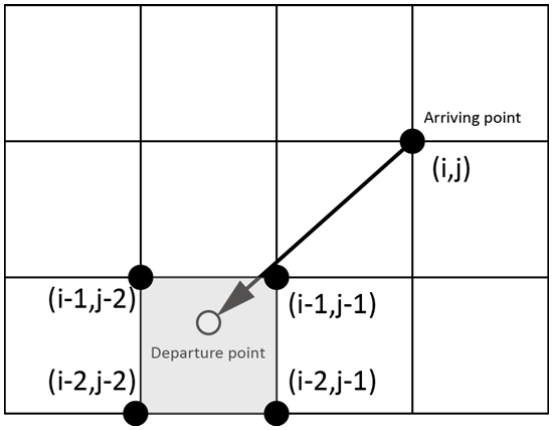

Figure 4 Schematic of Semi-Lagrangian scheme

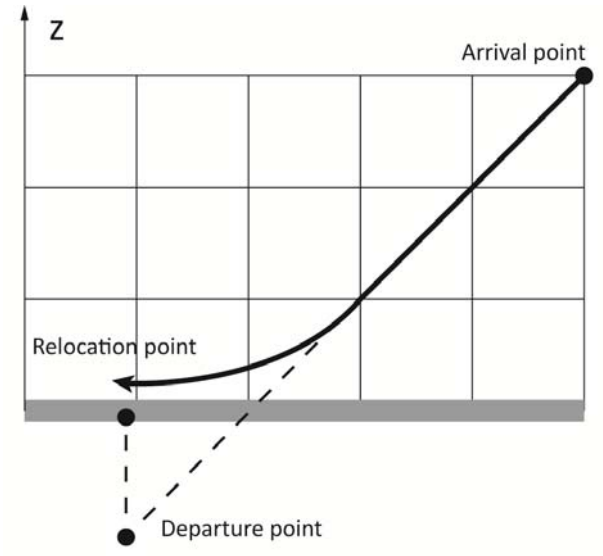

(a)

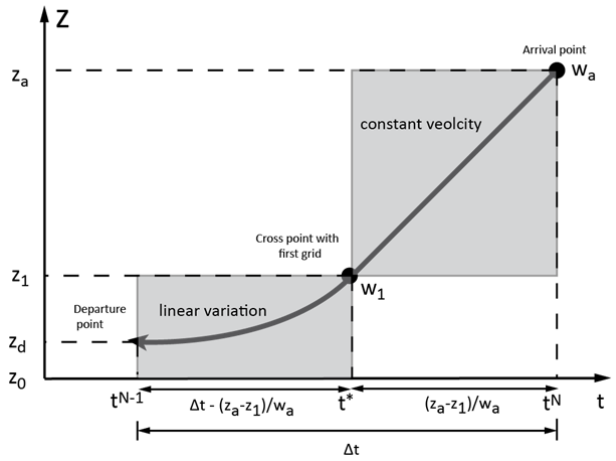

(b)

Figure 5 Schematic of near wall treatment for the Semi-Lagrangian scheme

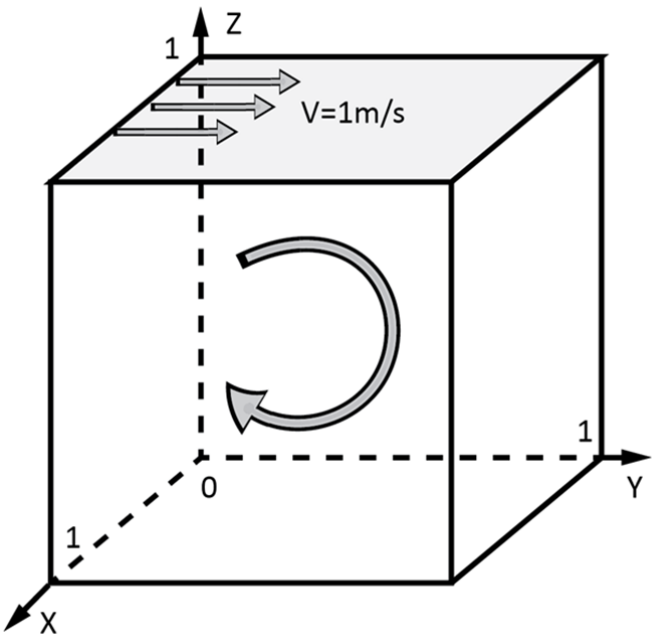

Figure 6 Schematic of the flow in cubic Lid-driven cavity

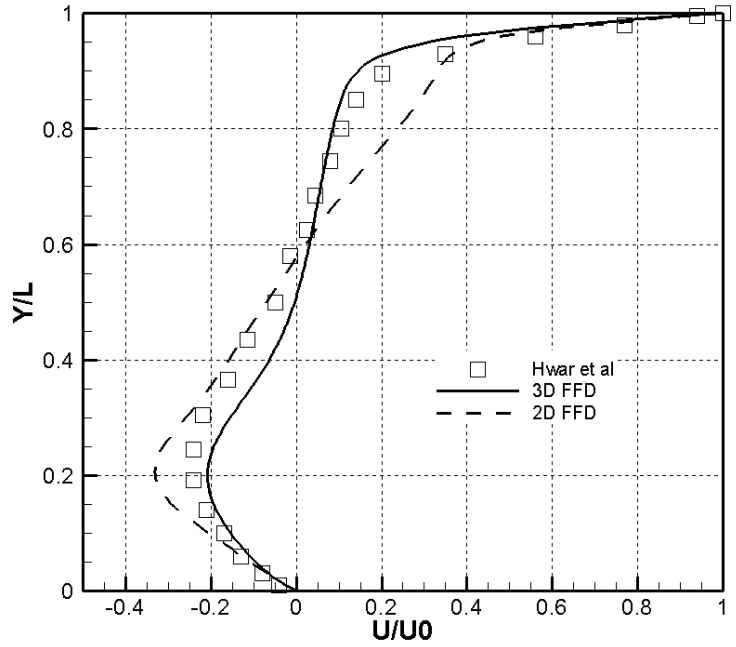

(a)

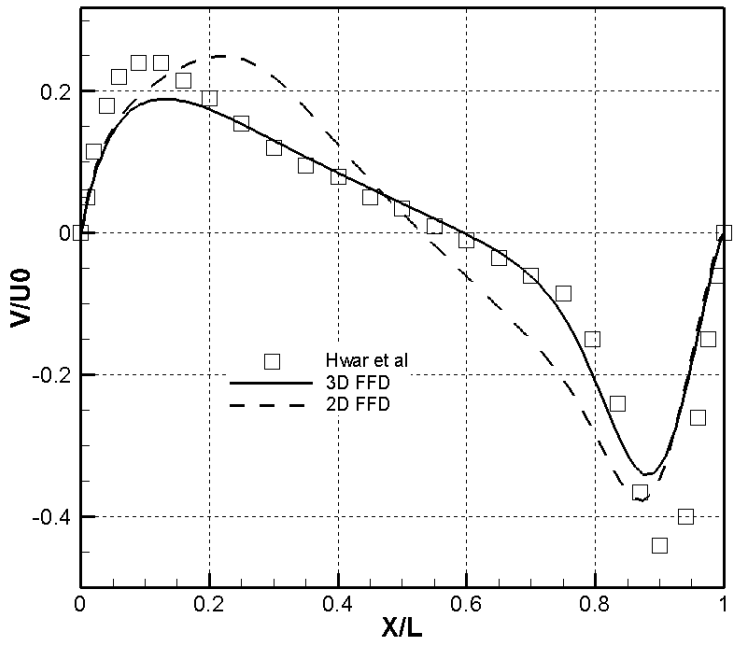

(b)

Figure 7 Comparison of velocity variation in the lid-driven cavity predicted by 3D FFD and 2D FFD with data from Ku et al. [15]: (a) vertical centerline and (b) horizontal centerline

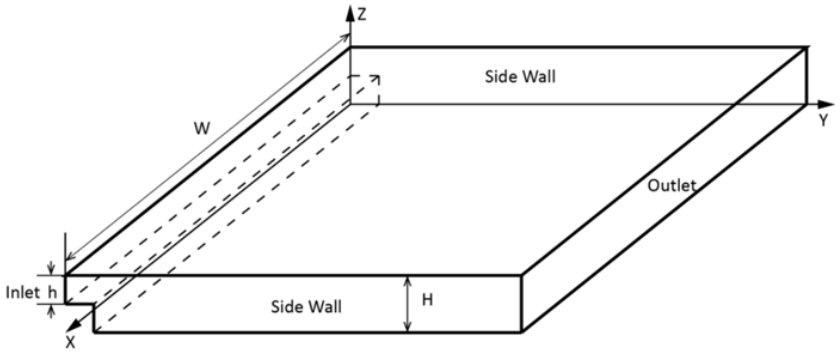

Figure 8

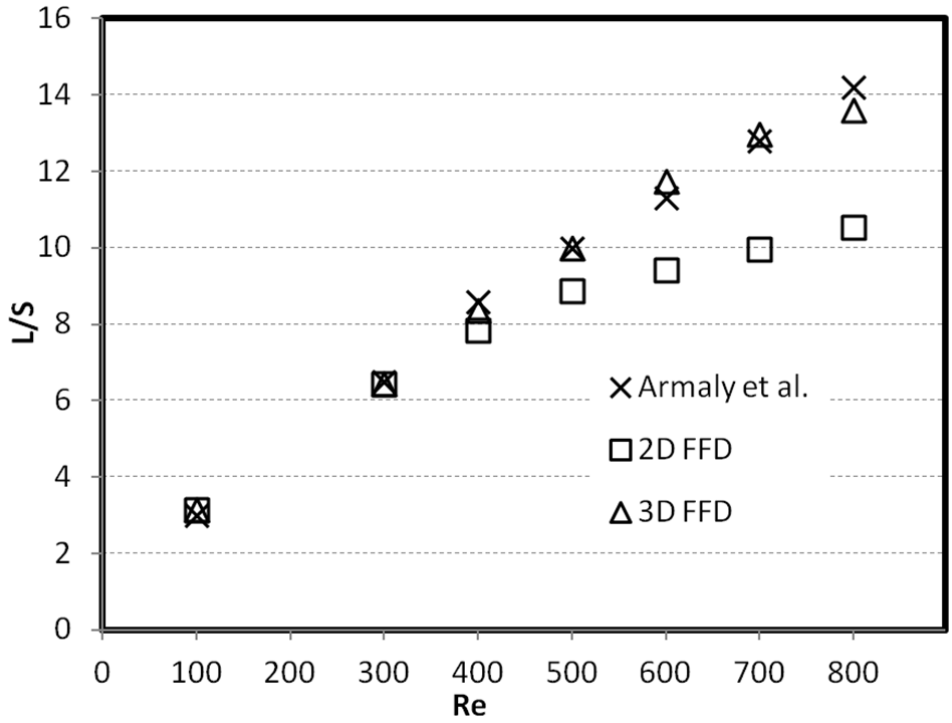

Figure 8 Comparison of primary reattachment length predicted by 3D FFD and 2D FFD with the data from Armaly et al. [16]

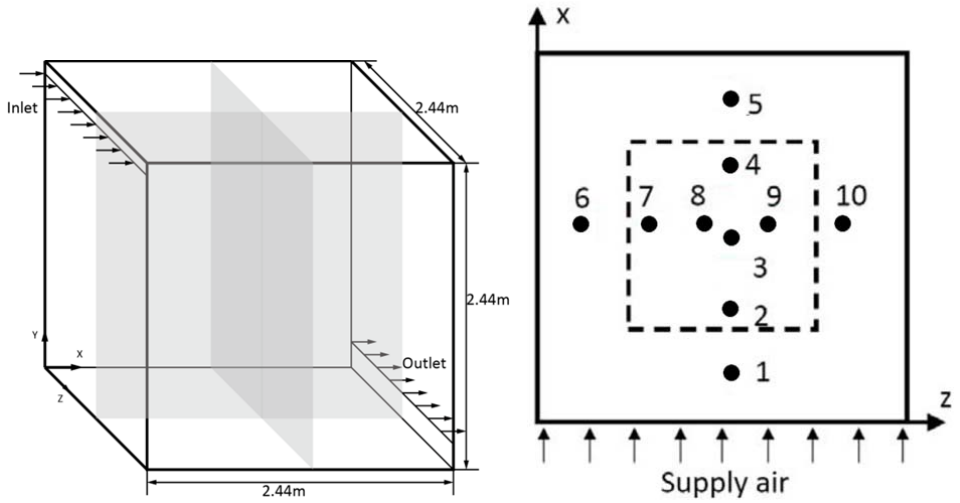

(a) (b)

Figure 9 Schematic of the test chamber for the forced convection and the measurement positions

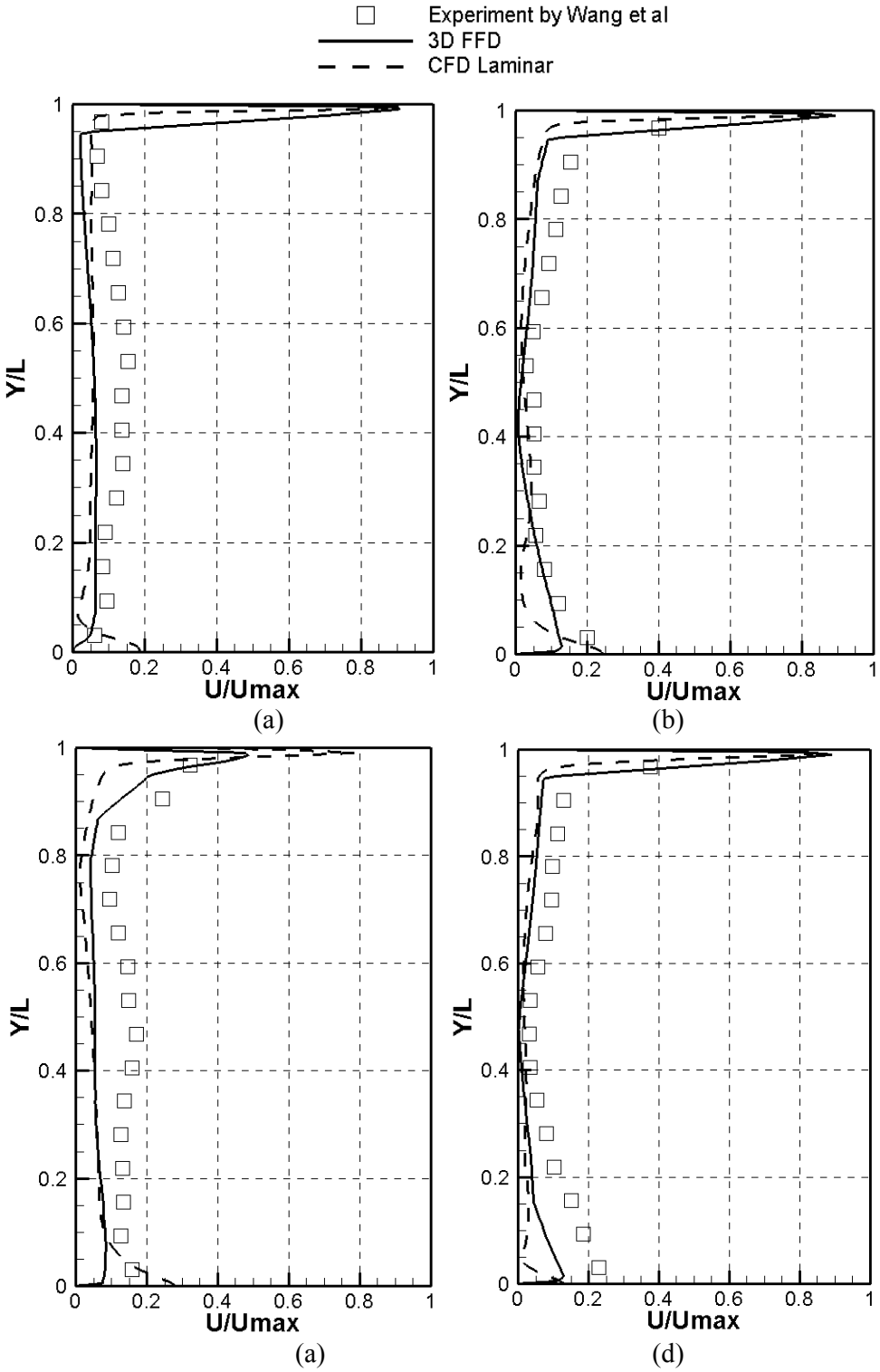

Figure 10 Comparison of velocity profiles in case A predicted by 3D FFD and CFD with the experiment data from Wang et al. [17] at positions (a) 1, (b) 3, (c) 5, and (d) 6, respectively

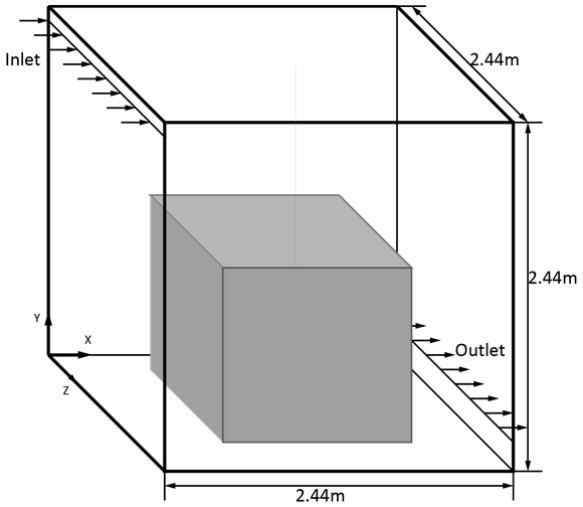
Inlet
2.44m
2.44m
Outlet
Y
X
Z
2.44m
Figure 12

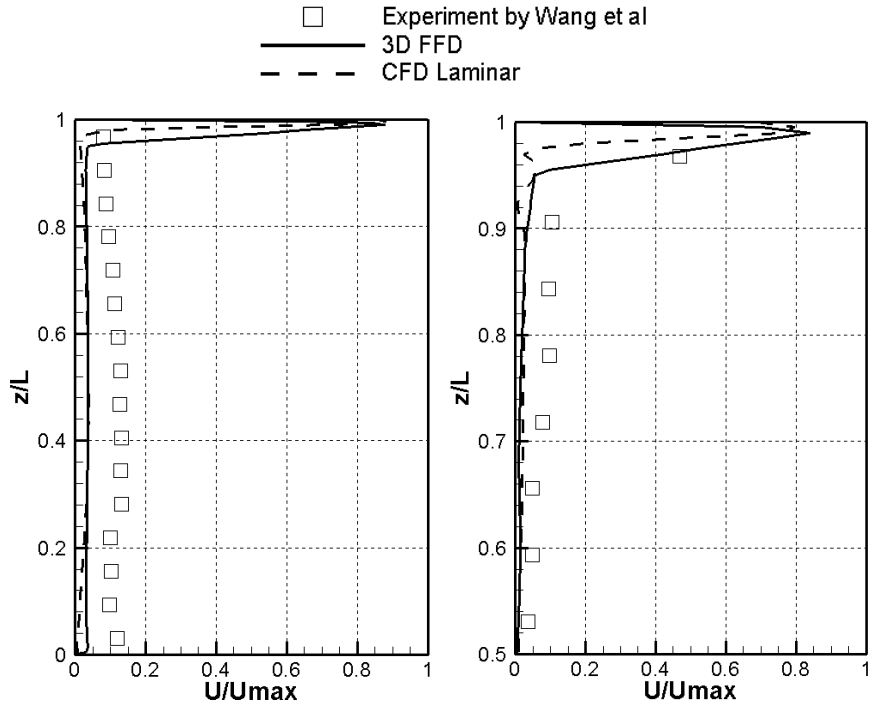
Experiment by Wang et al
3D FFD
CFD Laminar
z/L
U/Umax
z/L
U/Umax
(a) (b)

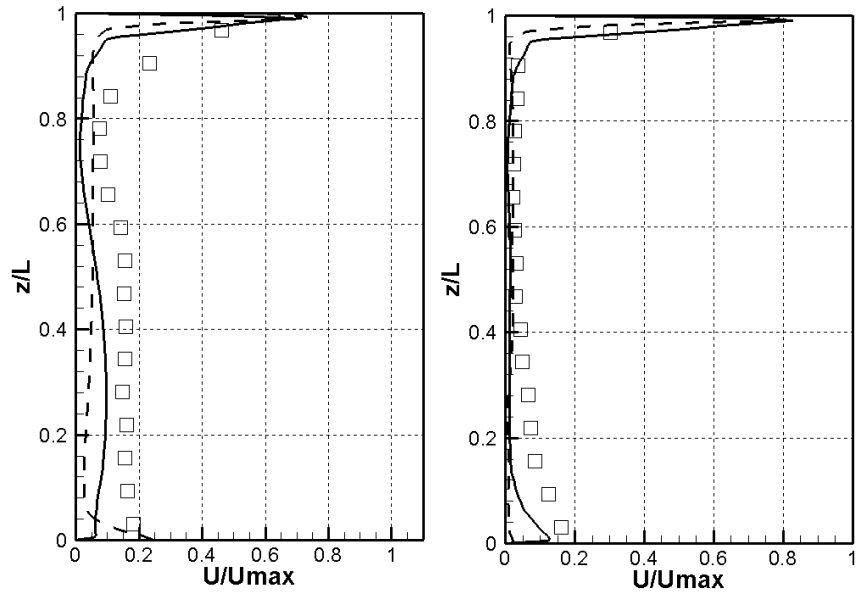

(c) (d)

Figure 11 Comparison of velocity profiles in case B predicted by 3D FFD and CFD with the experiment data from Wang et al. [17] at positions (a) 1, (b) 3, (c) 5 and (d) 6, respectively

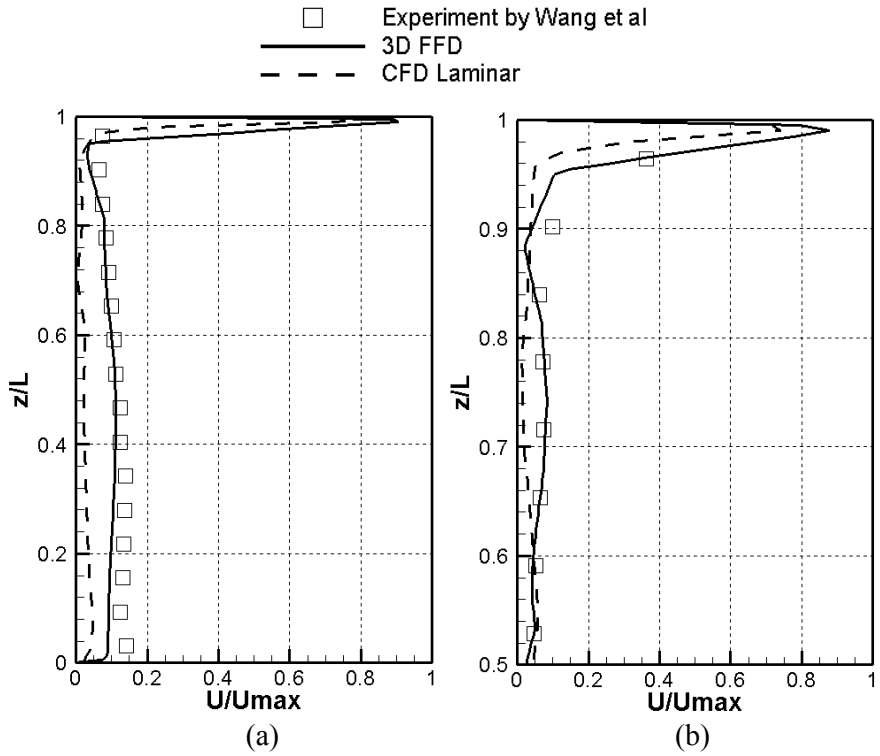

(a) (b)

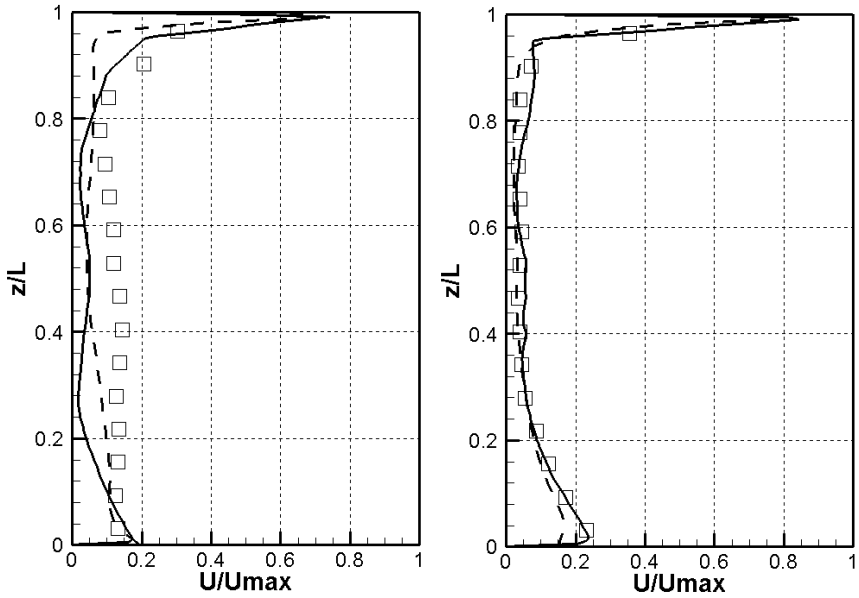

(c) (d)

Figure 12 Comparison of velocity profiles in case C predicted by 3D FFD and CFD with the experiment data from Wang et al. [17] at positions (a) 1, (b) 3, (c) 5 and (d) 6, respectively

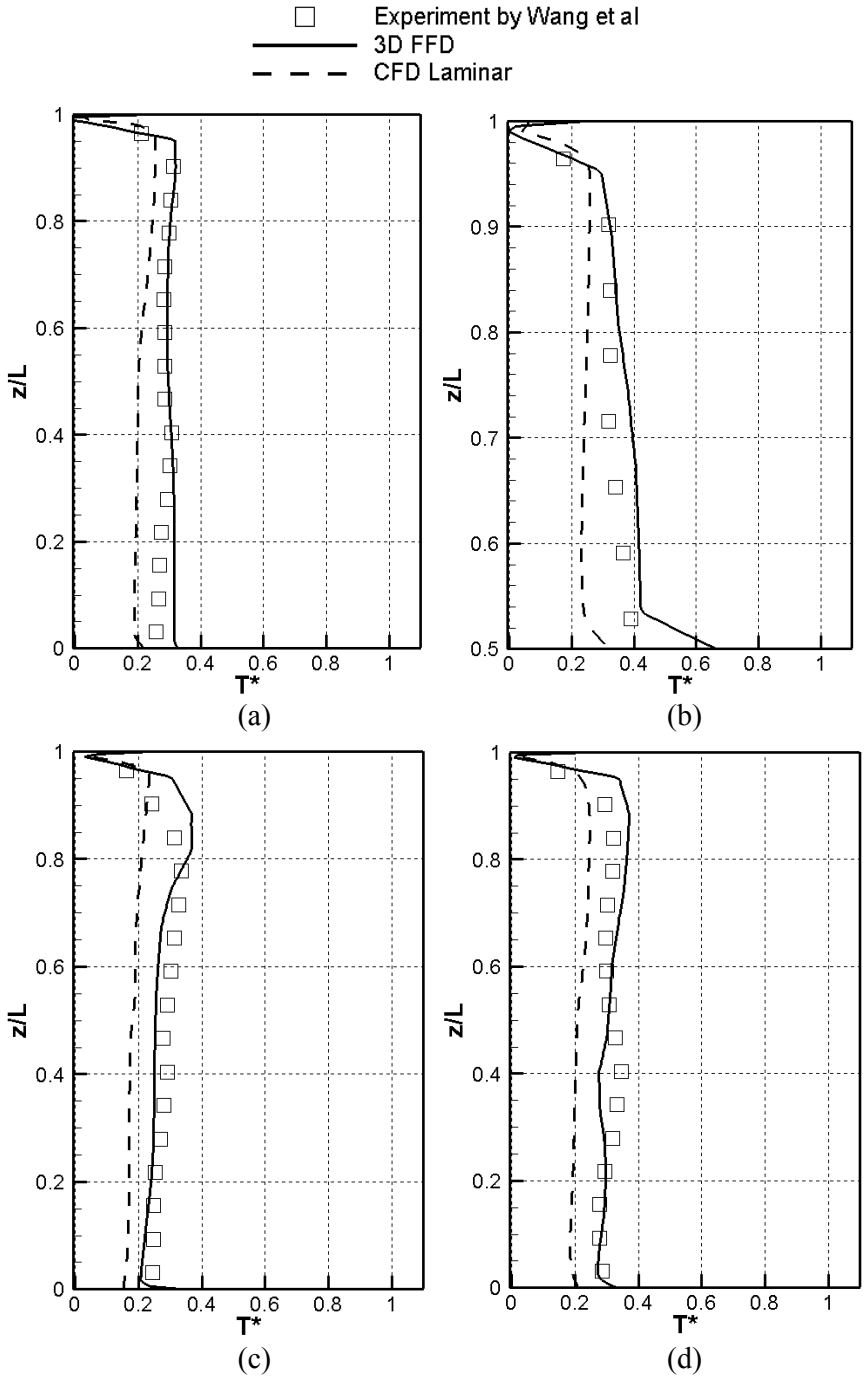

Figure 15